Chapter 43
Selected SEM and TEM Images by Late Dr. Hiroshi Nakahara

Mitsuo Kakei

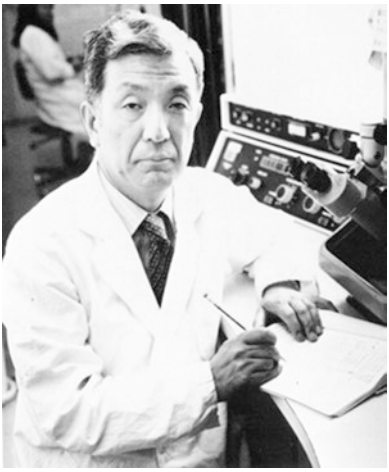

Dr. Hiroshi Nakahara (1928–2001)

Abstract The following SEM and TEM images were taken by late Dr. Hiroshi Nakahara many years ago, left unpublished, and shown on the screen during lunch-times in the symposium. He graduated from the course of zoology of the Faculty of Sciences, University of Hokkaido, and studied abroad in the University of New York and School of Dentistry, University of Texas. After returning home, he taught oral anatomy at Meikai University, School of Dentistry (former Josai Dental University). Using electron microscopes both SEM and TEM, he studied the mineralization processes of a variety of shellfish as well as vertebral hard tissues such as tooth enamel, dentin, and bone.

Keywords Bone · Ligament · *Monodonta confusa* · Nacreous layer · Otolith · Pearl · *Pinctada fucata* · Prismatic layer · Tooth enamel

M. Kakei (✉)
Tokyo Nishinomori Dental Hygienist College, Tokyo, Japan
e-mail: mkakei@jcom.home.ne.jp

K. Endo et al. (eds.), *Biomineralization*,
https://doi.org/10.1007/978-981-13-1002-7_43

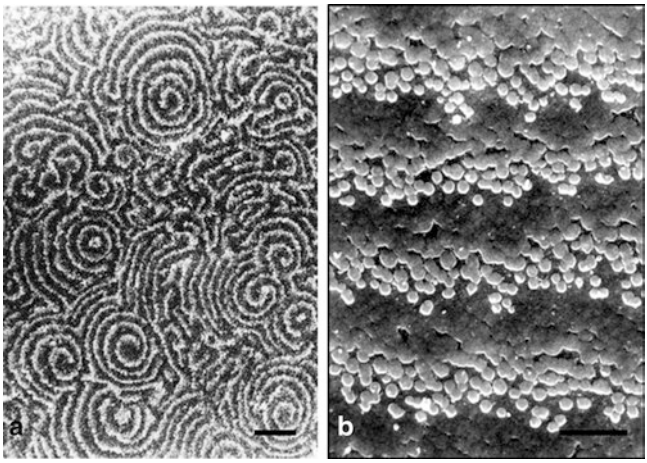

Fig. 43.1 SEM of growing surface of cultured pearl in *Pinctada fucata*. Spiral patterns are distributed across the surface (**a**). Aragonite tablets are arranged (**b**) (bars: **a** = 20 μm, **b** = 10 μm)

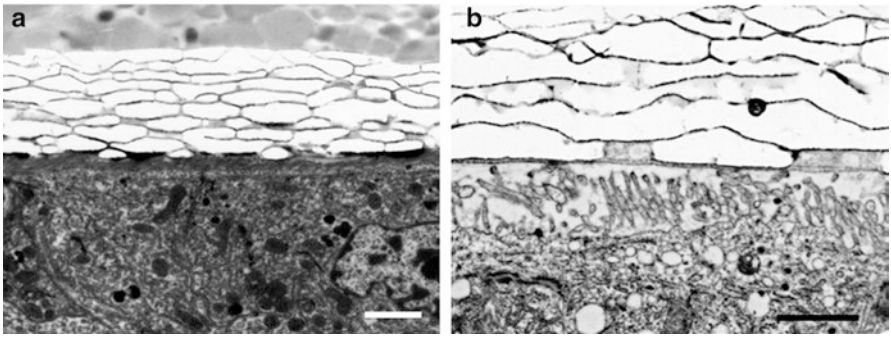

Fig. 43.2 TEM of nacre formation of *Pinctada fucata*. Growing surface of bivalve nacre is protected from being exposed to seawater by periostracum (bars: **a**, **b** = 2 μm, double staining)

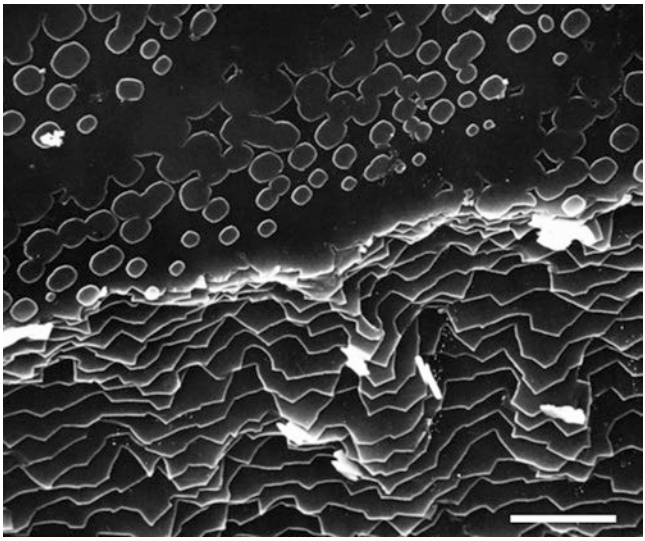

Fig. 43.3 SEM of the growing surface of nacreous layer of *Pinctada fucata*. The growing surface shows stepwise structure (bar: 5 μm)

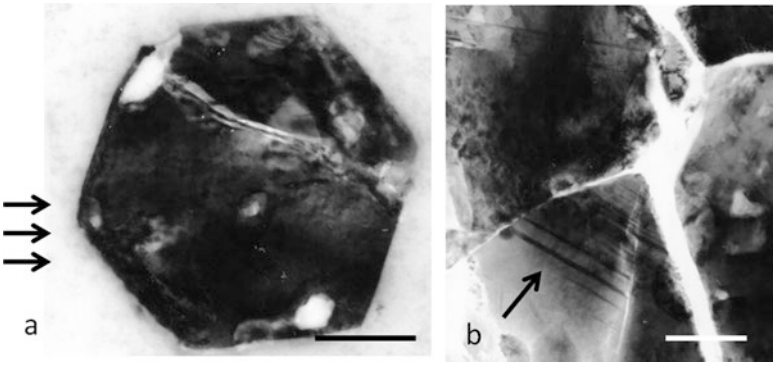

Fig. 43.4 TEM of a crystal in the nacreous layer of *Pinctada fucata*. Flat cut sections show polysynthetic twin (arrows) (bars: **a**, **b** = 500 nm)

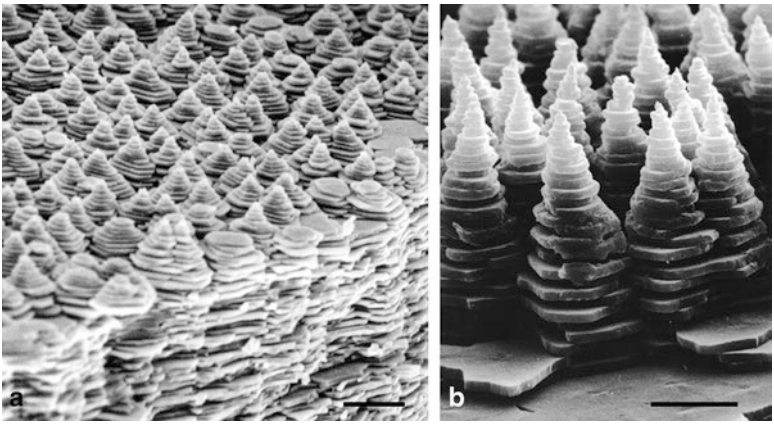

Fig. 43.5 SEM of growing surface of nacreous layer of *Monodonta confusa*. After treatment with sodium hypochlorite solution, columnar arrangement of tablets shows pyramid-shaped stacks (bars: **a** = 10 μm, **b** = 5 μm)

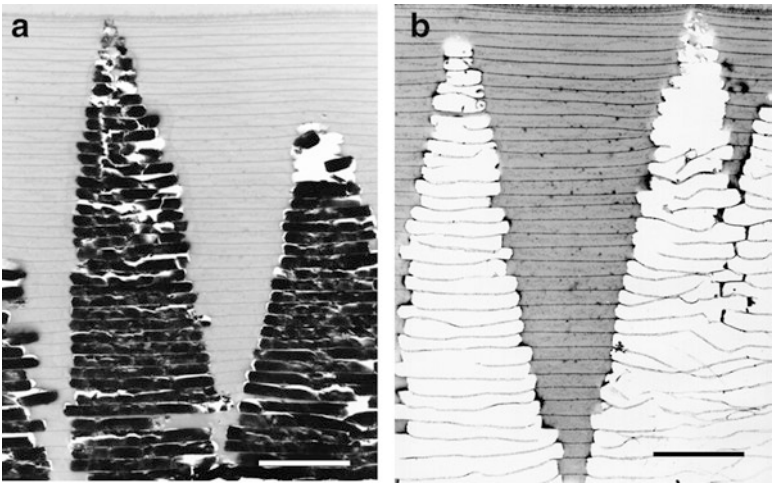

Fig. 43.6 TEM of growing surface of nacreous layer of *Monodonta confusa.* Tablets of crystals are created between the interlamellar matrix of sheets. (**a**) No staining, (**b**) double staining (bars: a, b = 5 μm)

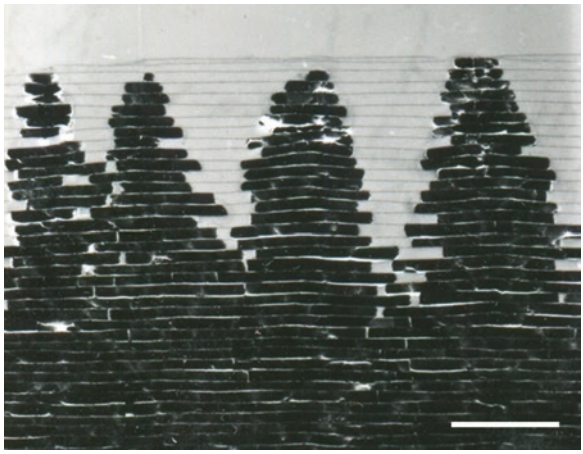

Fig. 43.7 TEM of growing surface of nacreous of *Sulculus diversicolor supertexta.* Crystals of snail nacre are arranged in the brick wall type, reinforcing the structural strength (bar = 5 μm)

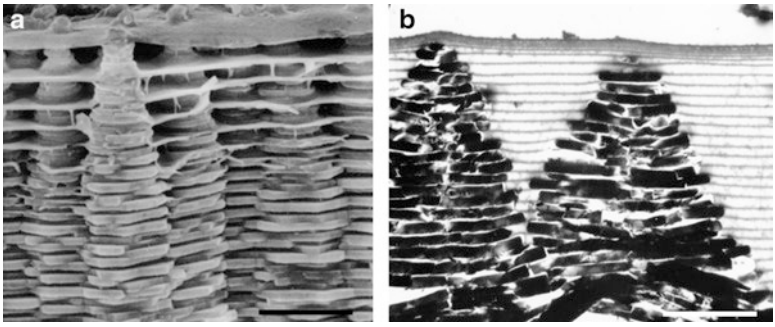

Fig. 43.8 SEM (**a**) and TEM (**b**) of the interlamellar matrix sheets of nacre of *Batillus cornutus*. Surface sheets cover the top of aragonite stacks (bars: **a** = 5 μm, **b** = 4 μm)

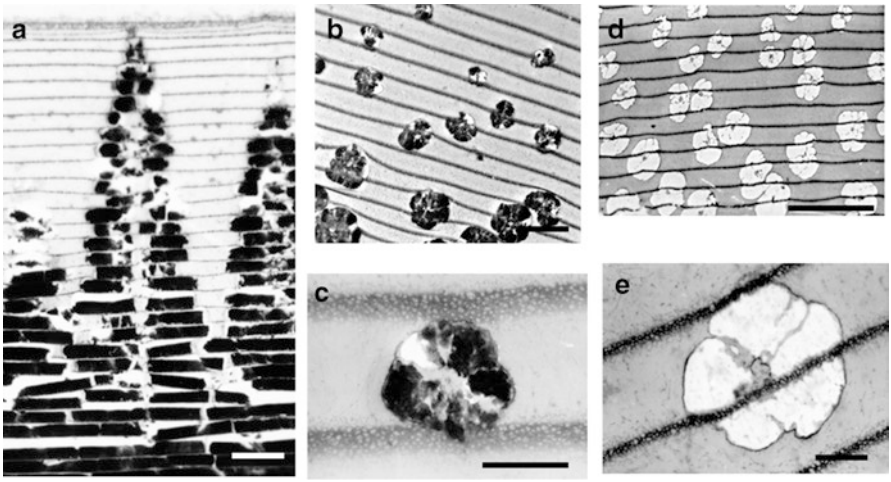

Fig. 43.9 TEM of nacre formation of *Calliostoma unicum*. (**a**) Central portion of the pyramid-shaped stacks shows empty space. (**b–e**) Sections were nearly parallel to the surface. Each tablet is divided into sectors (**b** and **c**). Organic cores remained at the center of stacks in the stained sections (**d** and **e**) (bars: **a** = 2.2 μm, **b** = 5 μm, **c** = 10 μm, **d** = 10 μm, **e** = 1 μm)

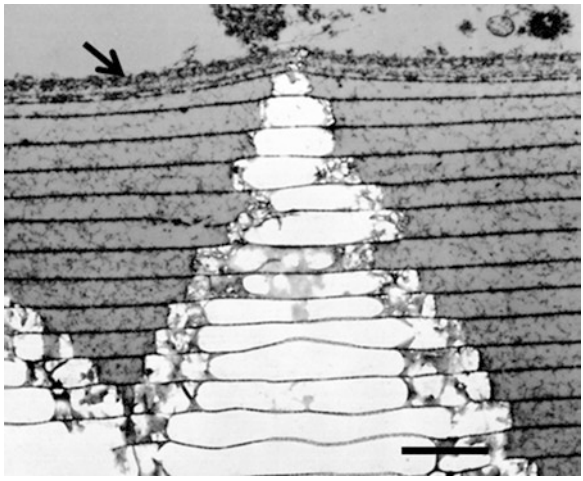

Fig. 43.10 TEM of nacre formation of *Batillus cornutus*. Thick surface sheet (arrow) is only formed in the gastropods and protects the developing nacre surface from seawater (double staining, bar = 10 μm)

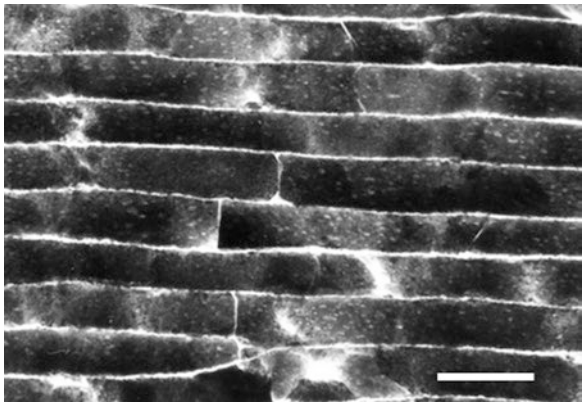

Fig. 43.11 TEM of transverse plane of nacreous layer of *Haliotis*. Brick wall-type structure enhances the structural strength (bar = 1 μm)

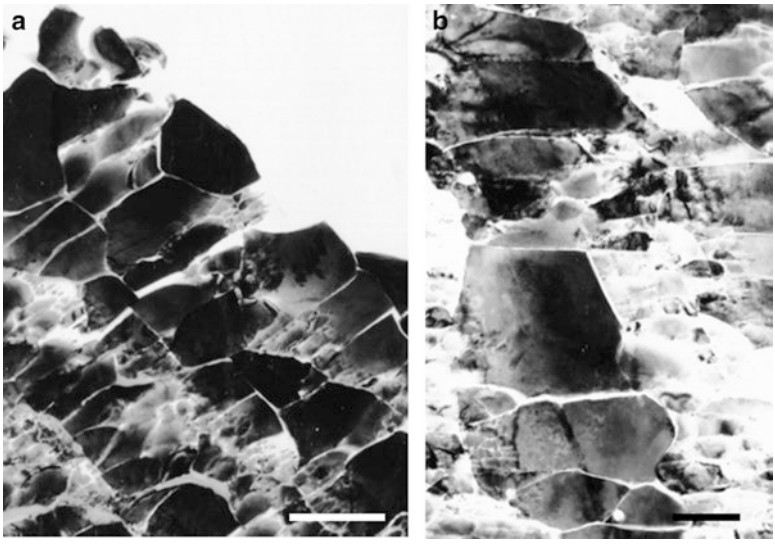

Fig. 43.12 TEM of nacre of *Lithophaga*. Flat-cut crystals are observed without staining (bars: **a** = 2 μm, **b** = 1 μm)

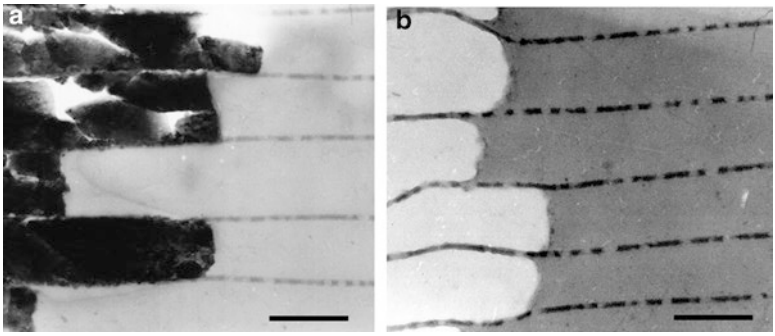

Fig. 43.13 TEM of nacre of *Sulculus diversicolor supertexta*. Thin sections show holes in the interlamellar matrix of organic sheets. (**a**) No staining, (**b**) double staining (bars: **a**, **b** = 1.0 μm)

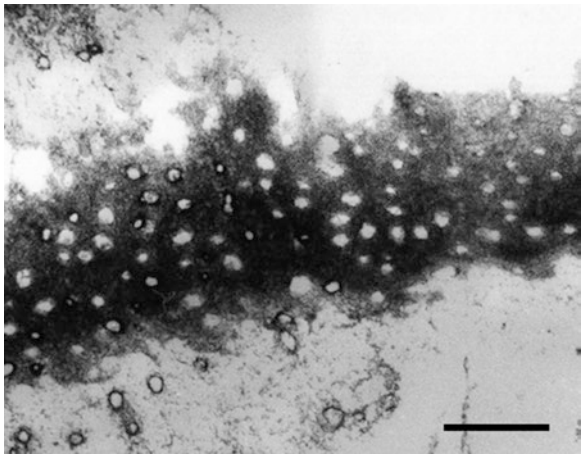

Fig. 43.14 TEM of the organic sheet of nacre of *Batillus cornutus*. Holes in the sheets are clearly observed in section cut to nearly parallel to the interlamellar matrix of sheets (bar = 250 nm)

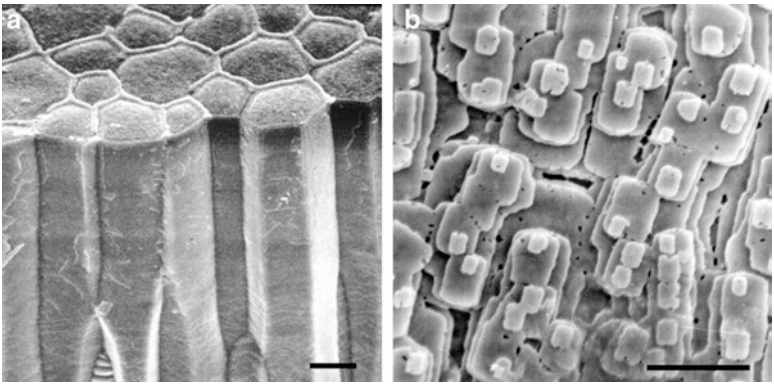

Fig. 43.15 SEM of the prismatic and nacreous layers of *Atrina pectinata*. Crystals of bivalve prismatic layer are arranged in a columnar fashion. (**a**) Crystals of the prismatic layer show rectangular shape. (**b**) Crystals of the nacreous layer (bars: **a** = 10 μm, **b** = 5 μm)

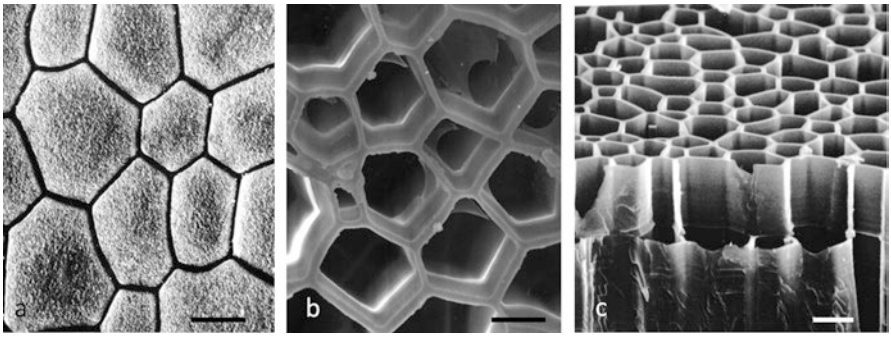

Fig. 43.16 SEM of the prismatic layer of *Pinctada fucata*. After acid treatment of (**a**), interprismatic layers remain as shown in Figs. (**b**, **c**). (**a**) Before decalcification, (**b, c**) after decalcification (bars: **a**, **b**, **c** = 10 μm)

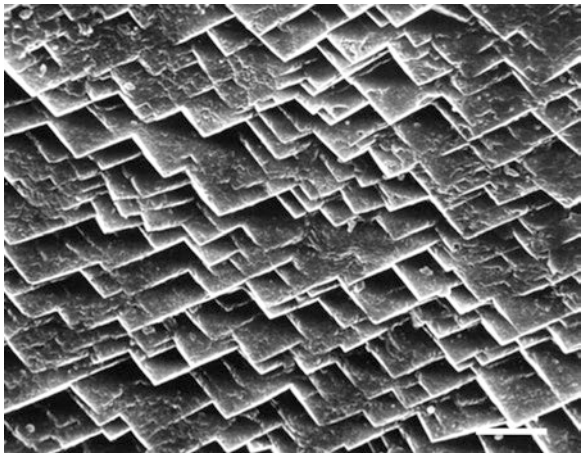

Fig. 43.17 SEM of the prismatic layer of *Cellana toreuma*. Imbricated pattern of mineral plates is observed (bar: 2 μm)

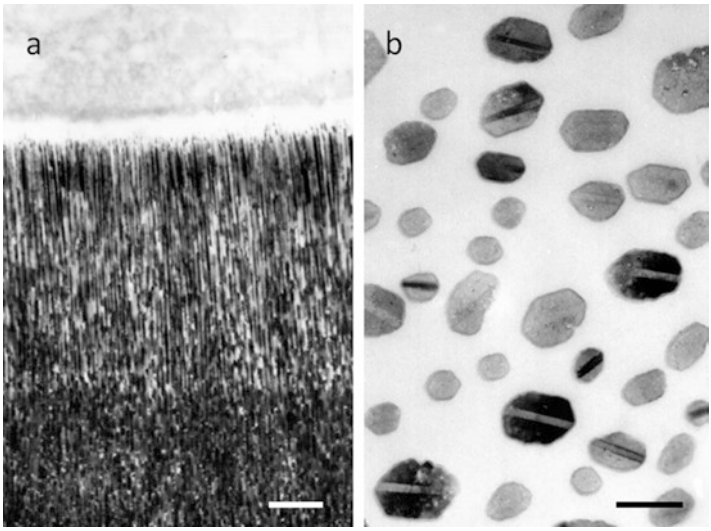

Fig. 43.18 TEM of aragonite crystals in the ligament of *Meretrix lusoria*. (**a**) Longitudinal section of crystals runs parallel with each other. (**b**) Cross section of the crystals shows hexagonal structure (bars: **a** = 2 μm, **b** = 1 μm)

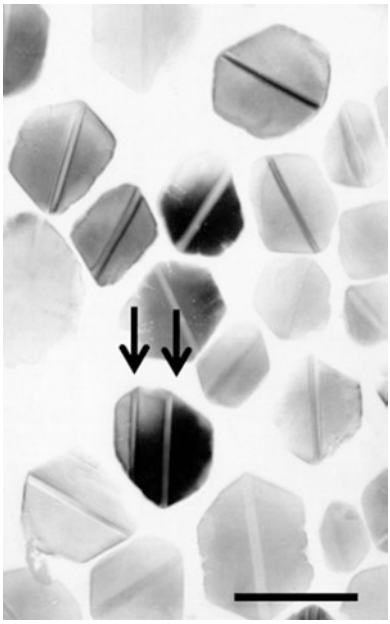

Fig. 43.19 Cross section of aragonite crystals in the ligament of *Neotrigonia* sp. Arrows indicate the polysynthetic twin structure (bar: 200 nm)

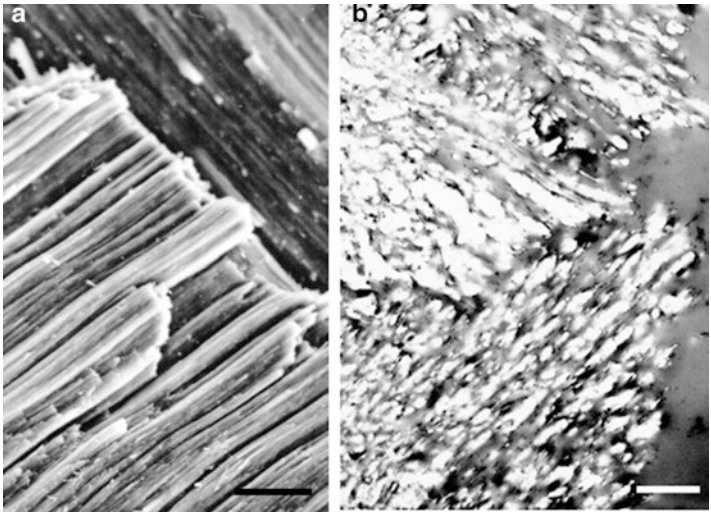

Fig. 43.20 SEM (**a**) and TEM (**b**) show the crossed lamellar structure of *Strombus gigas* (**b** double staining) (bars: **a** = 10 μm, **b** = 1 μm)

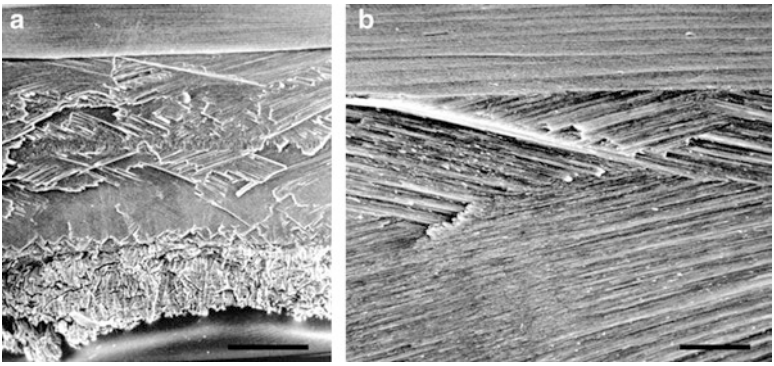

Fig. 43.21 SEM of the fracture surface of *Patelloida saccharina*. Long and thin aragonite crystals form a cross-lamellar structure (bars: **a** = 100 μm, **b** = 10 μm)

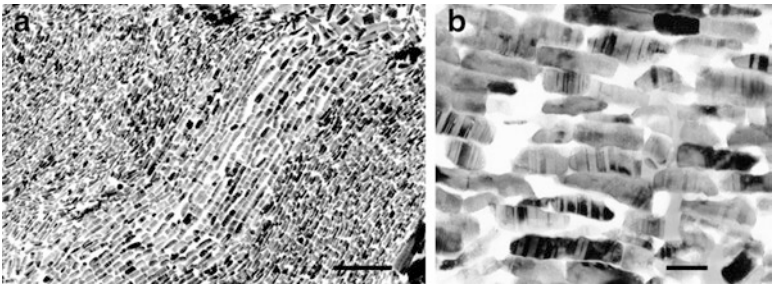

Fig. 43.22 TEM of aragonite crystals of *Patelloida saccharina*. (**a**) The cross section shows rectangular shape. (**b**) Crystals show twin pattern (bars: **a** = 1 μm, **b** = 110 nm)

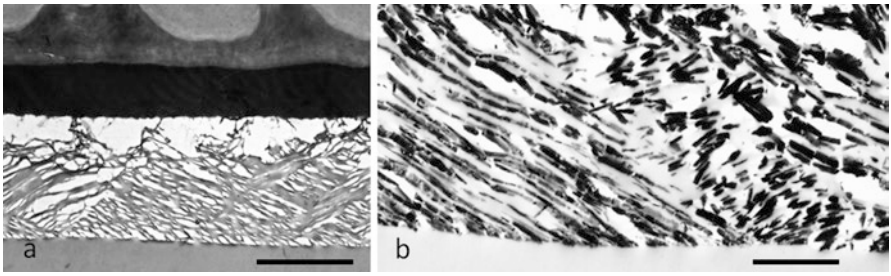

Fig. 43.23 TEM of shell of *Euhadra peliomphala*. The shell shows crossed-lamellar structure (**a** double staining, **b** no staining, bars: **a** = 5 μm, **b** = 2 μm)

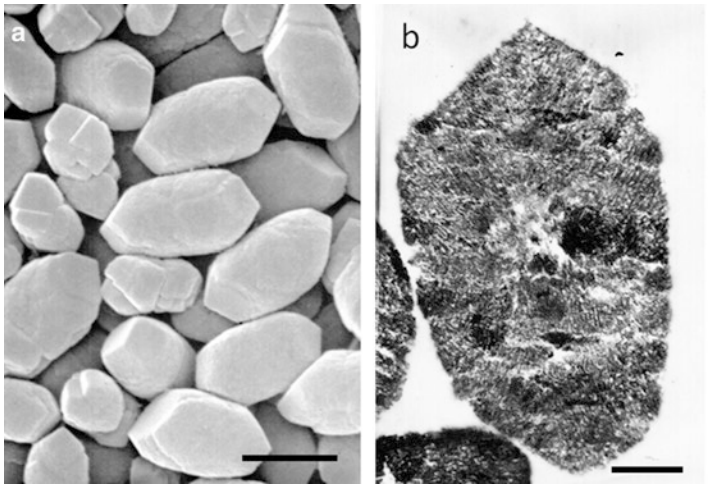

Fig. 43.24 SEM and TEM of otoliths of mouse. (**a**) SEM of both ends shows triangular in shape, and side view looks like cylindrical shape. (**b**) TEM of thin section without staining demonstrates that fine road-like crystals are arranged in a radial pattern (bars: **a** = 1 μm, **b** = 540 nm)

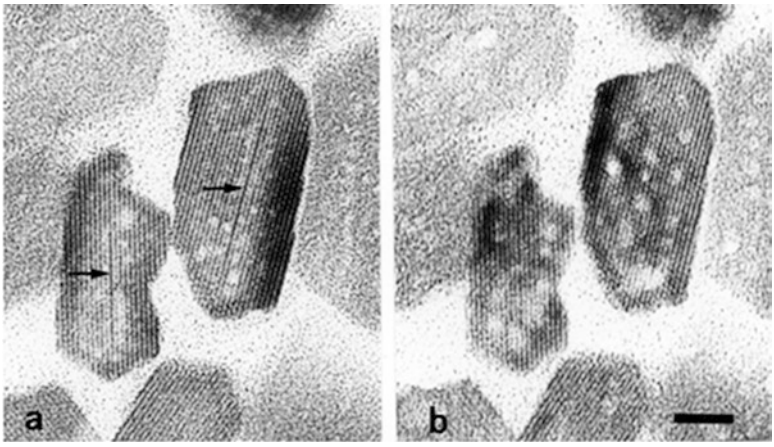

Fig. 43.25 TEM of apatite crystals of the rat tooth enamel. Central dark lines (arrows) do not create two lattice lines after electron beam exposure, showing a different physical property of octacalcium phosphate (**a** before beam damage, **b** after beam damage, bar = 10 nm)

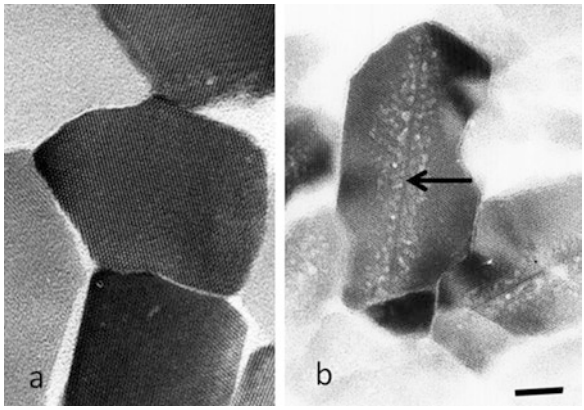

Fig. 43.26 TEM observations of shark enameloid (**a**) and rat tooth enamel (**b**) crystals. Cross sections show two different crystal characters, indicating two different mechanisms of crystal formation. Arrow: central dark line (CDL) (bar = 10 nm)

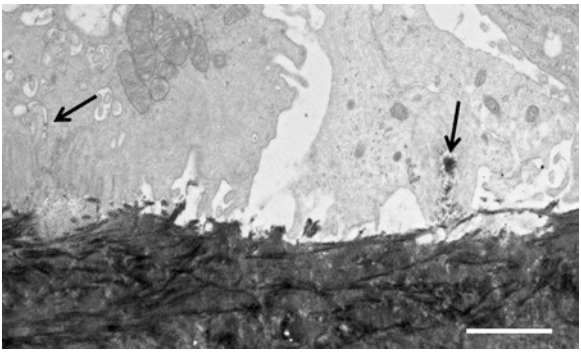

Fig. 43.27 TEM of bone resorption by osteoclast in rat. Arrows show that bone crystals were resorbed by endocytosis (bar = 2 μm)

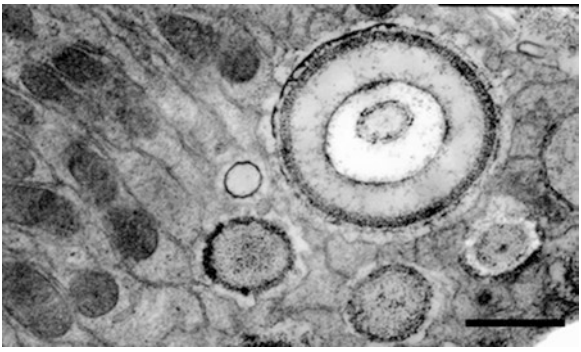

Fig. 43.28 TEM of Malpighian tubule of *Drosophila melanogaster*. Minerals of calcospherite are formed (bar = 1 μm)